




Magnetotransport properties of the topological semimetal SrAgBi

M. K. Hooda ¹, O. Pavlosiuk ², Z. Hossain,^{1,2} and D. Kaczorowski ²

¹Department of Physics, Indian Institute of Technology, Kanpur 208016, India

²Institute of Low Temperature and Structure Research, Polish Academy of Sciences, ulica Okólna 2, 50-422 Wrocław, Poland



(Received 28 January 2022; revised 15 April 2022; accepted 24 June 2022; published 7 July 2022)

Recently, the hexagonal compound SrAgBi has been theoretically predicted to host linearly dispersing type-II and nonlinearly dispersing type-IV Dirac fermions near the Fermi level. Here, we report the results of magnetotransport measurements performed on SrAgBi single crystals in the temperature range 2–300 K, with electric current flowing within the crystallographic *ab* plane and magnetic field up to 9 T oriented along the *c* axis. The electrical resistivity shows a metallic behavior, and an onset of filamentary like, type-II superconductivity below 2.9 K. The transverse magnetoresistance is positive and very small (approximately 4% at 5 K and 9 T). In weak fields and at low temperatures, it shows the existence of weak antilocalization effect, which signifies the presumed Weyl semimetallic character of SrAgBi. The Hall measurements show holes to be major charge carriers in the entire temperature range investigated. At 5 K, their density equals $\sim 5.4 \times 10^{20} \text{ cm}^{-3}$ and their mobility is $\sim 3.6 \times 10^2 \text{ cm}^2/(\text{V s})$. Based on the collected magnetotransport data, SrAgBi can be categorized as an uncompensated semimetal with the electrical properties describable using the simplistic single-band approach. The experimental results, in conjunction with the theoretical calculations, suggest that the topological surface states in SrAgBi are overshadowed by the large hole pocket which governs the transport behavior in this material.

DOI: [10.1103/PhysRevB.106.045107](https://doi.org/10.1103/PhysRevB.106.045107)

I. INTRODUCTION

In the last decade, there has been a flurry of theoretical and experimental investigations aimed at exploration of topologically nontrivial materials [1–9]. Among them, the topological semimetals (TSMs) are of special fundamental interest. Until now, various categories of TSMs have been discovered, such as Dirac, Weyl, nodal line, and triply degenerate nodal line semimetals, where bulk conduction and valence bands cross each other at some discrete points or closed trajectories in the reciprocal space [6–9]. The crossings linearly disperse along all the momentum directions, and the presence of nearly massless Dirac fermions gives rise to various exotic transport properties, such as chiral magnetic anomaly, extremely large magnetoresistance (MR), negative longitudinal MR, weak antilocalization (WAL) effect, magnetic field induced metal-insulator transition, planar Hall effect, and topological superconductivity, etc. [6–18].

Recently, a class of TSMs has been identified theoretically, namely the hexagonal ternary compounds crystallizing with space group $P6_3/mmc$, in which Dirac points are protected by the combination of time reversal, inversion, mirror, and various rotational symmetries such as C_3 and C_6 [6,8,19–24]. Despite the very rich spectrum of various topological behaviors predicted for these systems, their experimental authentication in real materials is still lacking.

The bismuthide SrAgBi is a prominent representative of such hexagonal TSM ternaries. It was theoretically predicted to host type-II and type-IV Dirac points above the Fermi level (located at 104.3 and 37 meV, respectively), which are protected by the principal rotation axis symmetry existing along the Γ -A direction [6,21]. In order to probe the anticipated topological features of the compound, we explore its

magnetotransport properties in a wide range of temperatures and external magnetic fields. The experimental data indicate that SrAgBi is an uncompensated semimetal with no obvious manifestation of any nontrivial behavior, except for the WAL effect observed in fields smaller than 0.8 T. We suggest that the presumed Weyl effects in the electrical transport of this compound may be obscured by the predominance of hole carriers originating from a single pocket of the Fermi surface. Below 2.9 K, the investigated single crystals of SrAgBi demonstrate a broad superconducting transition that likely has an extrinsic filamentary nature.

II. EXPERIMENTAL DETAILS

SrAgBi single crystals were grown using the self-flux method. The starting materials, i.e., Sr, Ag, and Bi, were taken in a molar ratio of 1:1:4, respectively, and placed in an alumina crucible, which was then vacuum sealed into a quartz tube. The ampoule was heated in a resistance furnace up to 1050 °C and held at this temperature for 24 h. Subsequently, it was slowly cooled down to 400 °C at a rate of 2.5 °C/h. At this temperature, the tube was removed from the oven, and the flux was centrifuged. The so-obtained single crystals were up to 3 mm in length, 2 mm in width, and 1 mm in thickness. The SrAgBi crystals were found to degrade with time and therefore were stored in a glove box to minimize the exposure to air before the measurements.

The hexagonal crystal structure of the obtained single crystals of SrAgBi (space group $P6_3/mmc$) was corroborated by x-ray diffraction (XRD) performed on single-crystalline specimens. Figure 1 shows an XRD pattern obtained from a top surface of one of the crystals that indicates a (00*c*) plane

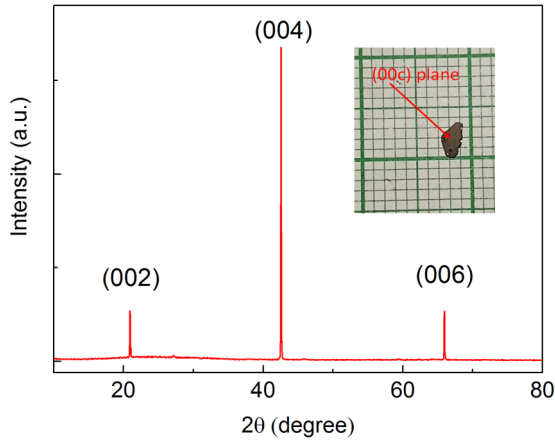


FIG. 1. Single crystal XRD pattern of SrAgBi. The inset shows a typical crystal grown from the Bi flux.

growth. Energy dispersive x-ray (EDX) spectroscopy measurements, done at several sites on a few individual crystals, confirmed the chemical composition close to 1:1:1 and fairly homogeneous elemental distribution (see Table I).

Magnetic properties were investigated in the temperature range 1.8–300 K using a Quantum Design MPMS-XL superconducting quantum interference device (SQUID) magnetometer. Heat capacity was measured in the temperature interval 2–300 K, employing the relaxation technique and two- τ model implemented in a Quantum Design PPMS-14 platform. Electrical transport studies were performed from 2 to 300 K in magnetic fields up to 9 T using a Quantum Design PPMS-9 platform. The electrical leads made of silver wires were attached to the bar-shaped specimens with silver-epoxy paste. The experiments were done employing a standard four-point ac technique. Several crystals were used for different measurements and they are denoted by C1, C2, C3, C4, C5, and C6 in the text.

III. RESULTS AND DISCUSSION

A. Transverse magnetoresistance

Figure 2 shows the temperature dependence of the electrical resistivity (ρ) of SrAgBi in zero magnetic field. It shows a regular metallic behavior down to about 2.9 K, and

TABLE I. Atomic percentage of each constituent in single-crystalline SrAgBi obtained from EDX done at different sites of a few crystals.

Site no.	Sr	Ag	Bi
1.	31.09	34.02	34.89
2.	32.85	31.62	35.52
3.	31.04	33.41	35.54
4.	31.84	34.14	34.01
5.	31.13	30.70	38.17
6.	31.21	32.74	36.05
7.	31.68	31.98	36.34
Average	31.55	32.66	35.78
Ratio	0.97	1	1.09

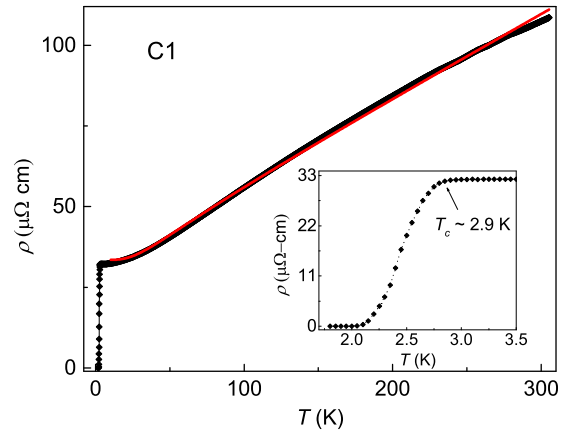


FIG. 2. Temperature variation of the electrical resistivity of single-crystalline SrAgBi measured within the hexagonal ab plane. Red line marks the BG fit described in the text. Inset: low-temperature resistivity data showing the superconducting transition below ~ 2.9 K.

at this temperature an onset of superconducting state was found (details provided in a separate section). At 300 K, the resistivity equals about $107 \mu\Omega \text{ cm}$, which is smaller than the magnitude of $150\text{--}750 \mu\Omega \text{ cm}$ reported in the literature for isostructural compounds [25,26]. With decreasing temperature, ρ decreases sublinearly and can be described by the standard Bloch-Grüneisen (BG) formula, $\rho(T) = \rho_0 + 4A\left(\frac{T}{\Theta_R}\right)^5 \int_0^{\Theta_R/T} \frac{x^5 dx}{(e^x - 1)(1 - e^{-x})}$, where ρ_0 stands for the residual resistivity due to scattering of conduction electrons on crystal lattice imperfections, Θ_R represents a characteristic temperature usually close to the Debye temperature, and A is a material dependent parameter. Fitting the BG function to the experimental data in the interval 15–300 K (see Fig. 2) yielded the values $\rho_0 = 33.5 \mu\Omega \text{ cm}$, $\Theta_R = 158.2 \text{ K}$, and $A = 40.8 \mu\Omega \text{ cm}$. These values are of the same order of magnitude as those values obtained for CaAgBi [9]. Below 15 K, $\rho(T)$ departs from the BG formula, and instead of T^5 dependence it follows nearly T^3 dependence, characteristic of Mott-type s - d interband scattering, and reported also for topological semimetals [27].

Figure 3(a) shows the transverse magnetoresistance of SrAgBi measured at several temperatures with magnetic field applied along the crystallographic c axis. At each temperature, MR is positive and in fields stronger than 0.8 T it follows a power law of $B^{1.7}$ (see also the Kohler plot displayed in the inset to this figure) without any tendency towards saturation up to 9 T. While for perfectly compensated semimetals, a quadratic field dependence of MR is usually observed [28], deviation from this standard behavior hints at dominance of one type of charge carrier. Another indication of the uncompensated charges in SrAgBi is a magnitude of MR that is as small as approximately 4% at $T = 5 \text{ K}$ in $B = 9 \text{ T}$, i.e., much smaller than MR observed for archetypal TSMs such as NbP, TaP, TaAs, and Cd_3As_2 [10,28,29]. In turn, MR values fairly similar to that found for SrAgBi were reported recently for the isostructural Dirac semimetal SrAgAs [26].

The magnitude of MR can be strongly reduced due to several factors such as small residual resistivity ratio (RRR), small carrier mobilities or large difference in charge carriers

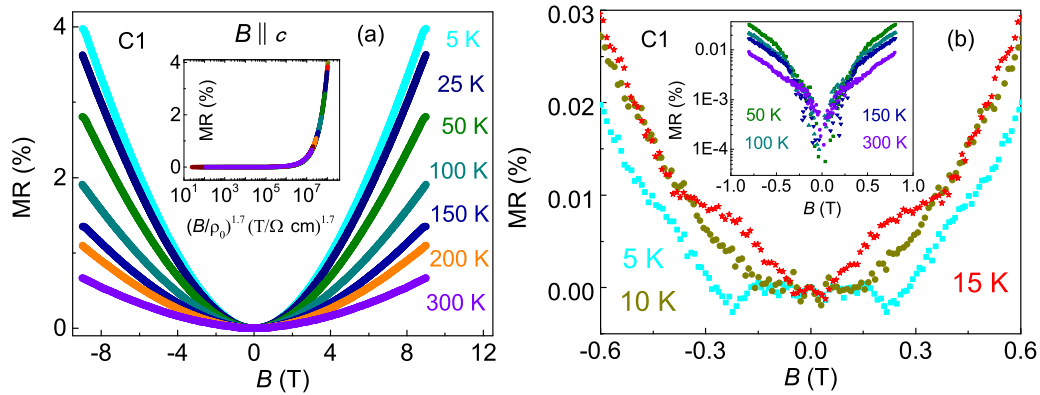


FIG. 3. (a) Transverse magnetoresistance isotherms of single-crystalline SrAgBi (crystal C1) measured within the hexagonal ab plane in magnetic field applied along the c axis. Inset: Kohler plot of the magnetoresistance data. (b) Low-field magnetoresistance data taken at temperatures from 5 to 15 K. Inset: low-field MR data measured at 50, 100, 150, and 300 K.

mobilities, and/or significant deviation from perfect electron-hole compensation [30–33]. In the case of the investigated crystals of SrAgBi, RRR of about 4 (see Table II) is small yet comparable to the values reported for TSMs, which exhibit relatively larger MR [18,29,34].

Figure 3(b) depicts the transverse MR data of SrAgBi measured in small magnetic fields. At 5 K, MR shows a flat inverted cusp for $B < 0.21$ T, which is a typical feature of weak localization (WL). In somewhat stronger fields, MR becomes positive and shows a sharp rise with increasing field that can be attributed to the WAL effect. The WL effect is observed to coexist with WAL up to 10 K. However above 10 K, the WL effect becomes insignificant and only the WAL effect is observed to persist. Previously, similar coexistence of the two quantum interference effects at low temperatures was observed in a few TSMs, such as PtPb₄, WTe₂, Sr₃SnO, TbPtBi, and DyPtBi, but also in ferromagnetic nanostructures (Ga,Mn)As or magnetically doped topological insulator Bi_{2-x}Cr_xSe₃ [35–40]. It is worthwhile to recall that the WL effect may originate from various phenomena like electron-electron interactions, intervalley scattering, structural disorder, or dominance of spin-flip relaxation time over dephasing time in charge scattering [36,37,41]. However, SrAgBi is a good metallic conductor, while strong electron-electron interactions and structural disorder typically result in the observation of negative coefficient of the electrical resistivity [37,41]. Hence, both phenomena can be ruled out as a possible source of WL in this compound.

Further, to confirm the coexistence and reproducibility of both WL and WAL, we performed low-field MR measurements on three additional SrAgBi single crystals, which are

TABLE II. The electrical resistivity, ρ of the five measured samples.

Sample	$\rho_{5\text{K}}$ (in $\mu\Omega\text{ cm}$)	$\rho_{300\text{K}}$ (in $\mu\Omega\text{ cm}$)	$\rho_{300\text{K}}/\rho_{5\text{K}}$
C1	32.1	107.5	3.35
C2	27	123.74	4.58
C3	101	348	3.44
C4	19	77.5	4.08
C5	34.3	155.25	4.53

denoted by C2, C3, and C4 in the text (see Fig. 4). It is interesting to note that all measured crystals do not exhibit the WL effect at low temperatures, as shown in Fig. 4. Crystal C2 shows the suppression in the magnitude of WAL below 25 K without any direct signature of WL as observed for the crystal C1. Another noted difference of crystal C2 is that it shows almost one order of magnitude higher MR value than the crystals C1, C3, and C4 in the WAL field range. However, at higher fields (outside the WAL effect field range), the increase in MR value slows down and is just a few times that of the other reported crystals as shown in bottom inset of Fig. 4(a). The presence of WL coexisting with WAL is much more apparent in crystal C3 at very low fields, which shows a MR value of less than 2.5% at 9 T and 5 K. On the other hand, crystal C4, which has smallest room-temperature resistivity value (see Table II) among the measured crystals, shows neither a suppressed WAL nor WL effect. The magnitude of WAL for crystal C4 shows a consistent decrease with increasing temperature [Fig. 4(c)]. It should be noted that MR data for the crystals C2, C3, and C4 exhibit a trend quite similar to the crystal C1 in higher fields (as shown by the red line fit in Fig. 4) and very persistent WAL effect in low fields.

It is clear from the presence of WL in some crystals and its absence in others that disorder plays a critical role in localization at low temperatures in SrAgBi, the amount of which differs from one crystal to another. Thus the interplay between the disorder and various other scattering rates (as discussed above) may be considered as a likely origin of the WL effect found in single-crystalline SrAgBi at low temperatures. The role of disorder scatterings in an induction of localization tendency in the Weyl semimetals is theoretically studied by Lu *et al.* [12]. While the WAL effect observed in SrAgBi single crystals is quite robust at low temperatures, its weak signature can be seen at somewhat higher temperatures as well, but is obscured by the classical MR contribution arising due to the Lorentz force.

In topological materials, WAL is caused by the presence of finite Berry phase in momentum space, which results from the spin-momentum locking in topological surface states (TSSs) [36]. In most TSMs, it is quite challenging to discriminate between the bulk and TSS contributions since the Fermi level

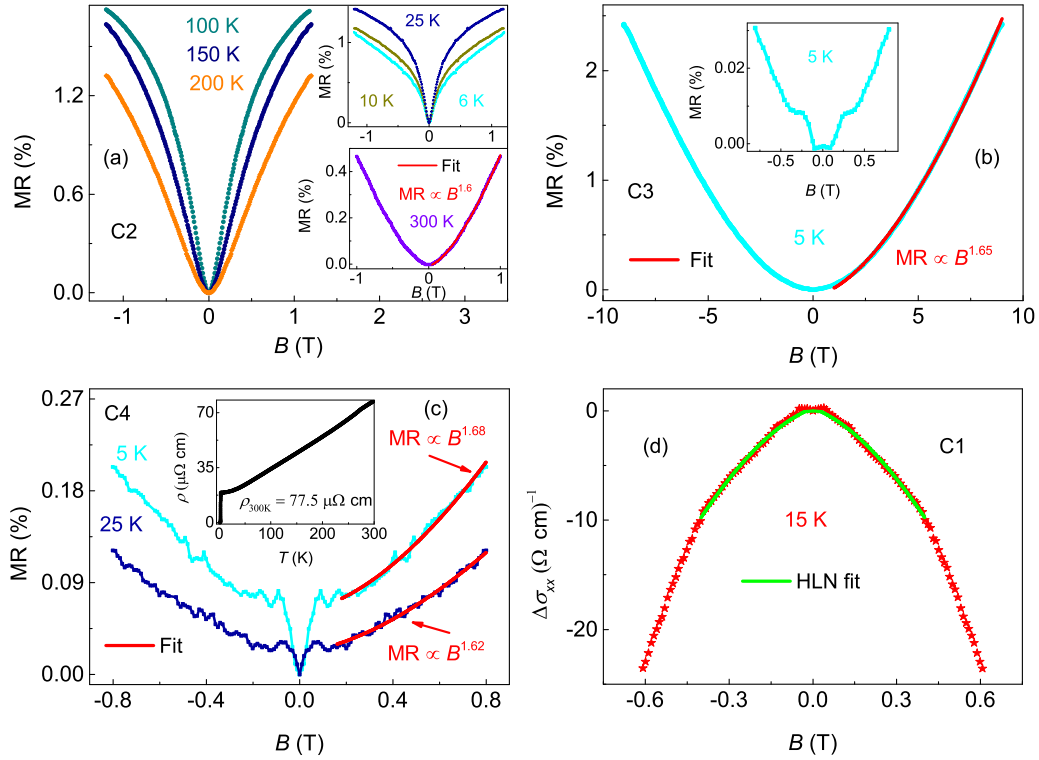


FIG. 4. Transverse magnetoresistance isotherms of the various single crystals of SrAgBi, marked by C2, C3, and C4 measured within the hexagonal ab plane in magnetic field applied along the c axis (a) Low-field magnetoresistance data for crystal C2 at temperatures of 100, 150, and 200 K. Top inset shows low-field magnetoresistance data at low temperatures of 6, 10, and 25 K. Bottom inset shows magnetoresistance data at 300 K with power law fit of $B^{1.6}$. (b) The magnetoresistance data for crystal C3 at 5 K in field range -9 to 9 T. The red line is fit to the data with power law of $B^{1.65}$ in fields higher than WAL range. Inset shows the zoomed view of low-field magnetoresistance data at 5 K. (c) Low-field magnetoresistance data for crystal C4 at 5 and 25 K. The red lines show the power law fit. Inset shows the electrical resistivity of crystal C4 in temperature 2 – 300 K at zero field. (d) Low-field magnetoconductivity data of crystal C1 measured at 15 K. Green line represents the HLN fit discussed in the main text.

crosses bulk bands, and bulk charge carriers usually also exhibit high mobility. In this respect, SrAgBi seems a fairly unique system showing rather low bulk carrier mobility (as indicated by the Hall data; see below), and Dirac points located close to the Fermi level [6]. According to the electronic band structure calculations, the compound harbors type-IV and type-II Dirac nodes situated at ~ 37 and 104.3 meV above E_F (along Γ -A direction), respectively. They are formed by three neighboring bands in the Brillouin zone located along the Γ -K-M and Γ -A directions. Remarkably, one of those bands forms a large sized hole pocket that governs the charge transport in SrAgBi (see below). Based on these findings, one can conclude that while TSSs contribute to the WAL effect in SrAgBi, the bulk contribution cannot be completely ignored.

The standard expression for the magnetoconductivity due to WAL ($\Delta\sigma_{xx}$) was formulated by Hikami, Larkin, and Nagaoka (HLN) [42]:

$$\Delta\sigma_{xx}(B) = -\frac{\alpha e^2}{2\pi^2\hbar} \left[\psi \left(\frac{\hbar}{4eL_\phi^2 B} + \frac{1}{2} \right) - \ln \left(\frac{\hbar}{4eL_\phi^2 B} \right) \right], \quad (1)$$

where α , e , ψ , and L_ϕ denote the number of conduction channels per unit length, elementary charge, digamma function, and phase coherence length, respectively. At low temperatures, the reliable fit of Eq. (1) is often difficult to achieve

due to some scatter in the experimental data taken in weak magnetic fields. For this reason, in the case of SrAgBi, we attempted to analyze the MR data measured at 15 K for crystal C1. An additional contribution from the spin-orbit and elastic scatterings is removed by adding an extra term $cB^{1.7}$ in Eq. (1). The result is shown in Fig. 4(d). The HLN fit yielded $L_\phi \approx 185$ nm and $\alpha \approx 1.34 \times 10^6$ m $^{-1}$. Using the sample thickness of 270 μ m, we estimated the total number of conduction channels in the SrAgBi crystal studied to be about 3.62×10^2 . This number is very small compared to the values reported for topological insulators LuPdBi, YPtBi, and topological nodal-line semimetal YbCdGe [43–45].

B. Hall resistivity

Figure 5(a) shows the Hall resistivity (ρ_{xy}) of single-crystalline SrAgBi measured within the hexagonal ab plane at a few selected temperatures as a function of magnetic field applied along the crystallographic c axis. Each Hall isotherm is a straight line, which indicates the dominance of one type of charge carriers. The positive sign of $\rho_{xy}(B)$ suggests that the electrical transport in SrAgBi is governed by holes. This finding is consistent with the uncompensated character of carriers deduced from the transverse MR data and the Kohler's plot.

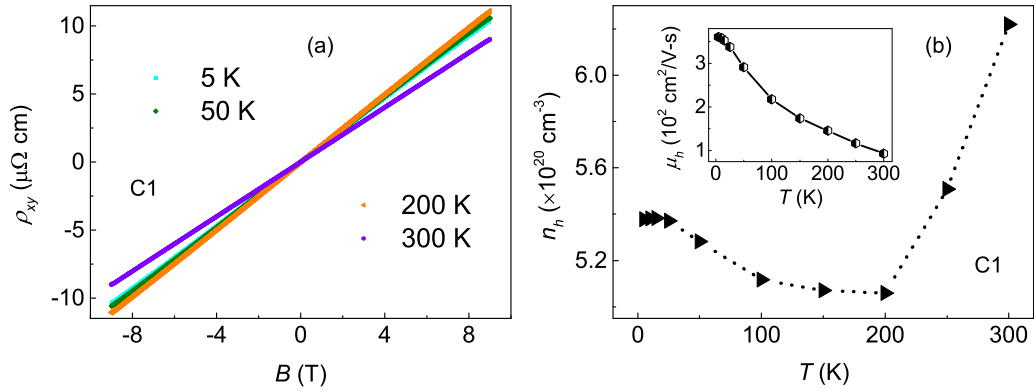


FIG. 5. (a) Field dependence of the Hall resistivity in single-crystalline SrAgBi shown at a few selected temperatures within the hexagonal ab plane with magnetic field aligned along the c axis. (b) Temperature dependence of the hole carrier density estimated from the Hall resistivity data. Inset: temperature dependence of the hole mobility.

In the next step, we employ the single-band model to extract the information on carrier density and mobility of charge carriers. The single-band model applies to those systems in which the contribution of one band dominates contributions due to other bands. Such systems are characterized by a single effective relaxation time or scattering rate of the charge carriers [46]. From fitting linear function to the $\rho_{xy}(B)$, the Hall coefficient (R_H) can be obtained. R_H does not depend on effective mass or relaxation time, but only on carrier concentration and sign of the charge carriers, $R_H = 1/en_i$, where n_i is the carrier concentration. The temperature dependence of the hole carrier density, n_h , is shown in Fig. 5(b). The estimated n_h is the order of $\sim 10^{20} \text{ cm}^{-3}$ in the whole temperature range, typical of semimetallic systems and comparable to n_h reported for CaAgBi [9]. In the range 5–15 K, n_h is nearly independent of T , but above 15 K, it decreases until a minimum is achieved at 200 K. Then, it increases up to room temperature. However, it should be noted that the overall change in the hole concentration between 5 and 300 K is very small (just $\sim 19\%$).

The hole carrier mobility, $\mu_h = R_H/\rho_{xx}(B=0)$ is shown in the inset of Fig. 5(b). The magnitude of μ_h decreases with increasing temperature and attains a value of $\sim 3.6 \times 10^2 \text{ cm}^2/(\text{V s})$ at 5 K that is almost two orders of magnitude smaller than that reported for uncompensated semimetals NbP and TaP, which exhibit extremely large MR at low temperatures [28] and one order of magnitude smaller than the values reported for SrAgAs [26].

C. Heat capacity

Figure 6 shows the temperature dependence of the specific heat (C_p) of SrAgBi. At 300 K, C_p equals $\sim 80 \text{ J}/(\text{mol K})$, which is close to the limit $3nR = 74.84 \text{ J}/(\text{mol K})$ (n is the number of atoms in formula unit, and R stands for the universal gas constant) predicted by Dulong-Petit law. As marked in Fig. 6 by the solid red curve, the experimental $C_p(T)$ data can be approximated by the Debye-Einstein (DE) formula,

$$C_p(T) = \gamma T + 9nR(1-d) \left(\frac{T}{\Theta_D}\right)^3 \int_0^{\Theta_D/T} \frac{x^4 e^x}{(e^x - 1)^2} dx + 3nRd \left(\frac{\Theta_E}{T}\right)^2 \frac{e^{\Theta_E/T}}{(e^{\Theta_E/T} - 1)^2}, \quad (2)$$

where the first term represents the electronic contribution (γ is the Sommerfeld coefficient), and the two successive terms account for the lattice contributions [Θ_D and Θ_E are the Debye and Einstein temperature, respectively, and the coefficients d and $(1-d)$ represent the respective Einstein and Debye phonon contributions, respectively]. Because the application of Eq. (2) was found inaccurate below 10 K, if γ was treated as a free parameter, it was estimated from fitting $C_p(T)$ in the interval $2 \text{ K} < T < 3.5 \text{ K}$ to the standard expression $C_p = \gamma T + \beta T^3 + \delta T^5$ (see the inset to Fig. 6). This way, the values $\gamma = 0.3 \text{ mJ}/(\text{mol K}^2)$, $\beta = 0.61 \text{ mJ}/(\text{mol K}^4)$, and $\delta = 0.17 \text{ mJ}/(\text{mol K}^6)$ were determined. The small value of γ reflects the small density of the electronic states at the Fermi level, which is a characteristic feature of semimetals. Recently, a similar magnitude of the electronic term in C_p was reported for nodal-line Dirac semimetals CaAgP and CaAgAs [47]. In the next step, Eq. (2) with fixed $\gamma = 0.3 \text{ mJ}/(\text{mol K}^2)$ was fitted to the specific heat data measured in the entire temperature range, and this analysis yielded the parameters $\Theta_D = 205.4 \text{ K}$, $\Theta_E = 50.2 \text{ K}$, and $d = 0.23$. The value of Θ_D is larger than Θ_R estimated from the BG fit of $\rho(T)$. The

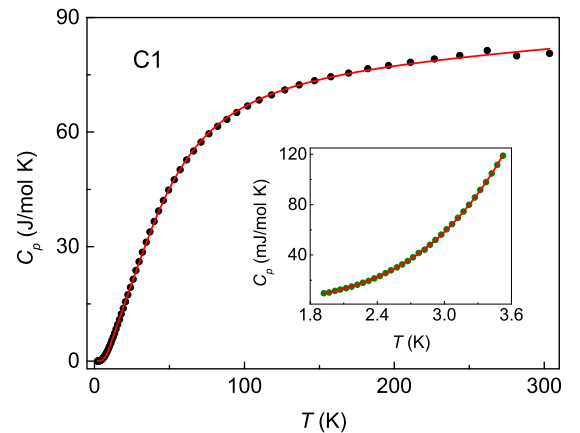


FIG. 6. Temperature dependence of the specific heat of SrAgBi. Solid red line represents the DE fit discussed in the text. Inset: low-temperature data. Solid red line corresponds to the fit specified in the main text.

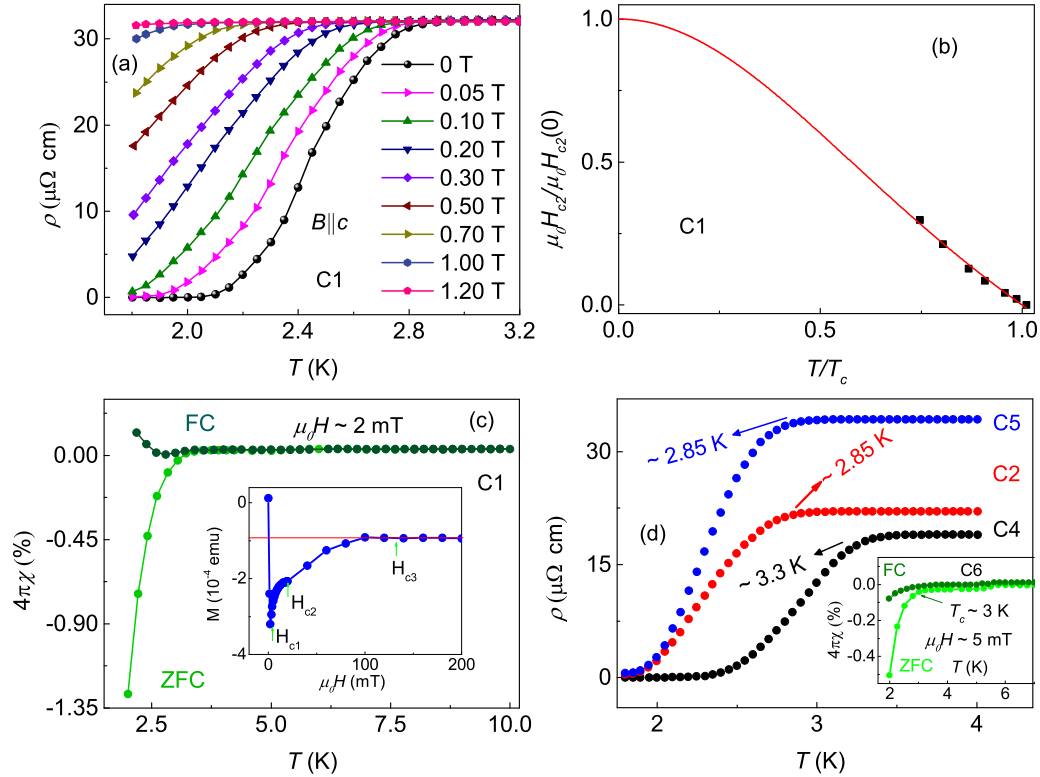


FIG. 7. (a) Temperature dependence of the electrical resistivity of single-crystalline SrAgBi (crystal C1) measured within the hexagonal ab plane in the region of the superconducting transition with magnetic fields applied parallel to the crystallographic c axis. (b) The normalized upper critical field as a function of the reduced temperature evaluated from the resistivity data. Solid red line represents the fit of the GL formula discussed in the text. (c) Low-temperature dependence of the magnetic susceptibility of single-crystalline SrAgBi measured in a magnetic field of 2 mT upon cooling the sample in zero (ZFC) and applied (FC) field mode. The data are represented as a superconducting volume fraction. Inset: field variation of the magnetization in single-crystalline SrAgBi determined at $T = 2$ K upon cooling the sample in zero field mode. Arrows indicate the critical fields $\mu_0 H_{c1}$, $\mu_0 H_{c2}$, and $\mu_0 H_{c3}$. (d) Low temperature electrical resistivity data at zero-magnetic field show the superconducting transition for three different crystals as marked by C2, C4, and C5. Arrows indicate the superconducting transition temperature. Inset displays the low-temperature dependence of the magnetic susceptibility (as a superconducting volume fraction) of a crystal C6 measured in a magnetic field of 5 mT in ZFC and FC mode.

difference between Θ_R and Θ_D is due to oversimplification of electron-phonon scattering process in the BG model, such as considering only longitudinal phonons, neglecting umklapp scattering, and assuming that conduction electron energy remains unchanged by scattering of phonons.

As can be inferred from the inset to Fig. 6, the specific heat of SrAgBi remains featureless down to 2 K. In particular, no anomaly arises near 2.9 K, where the onset of superconductivity was found in the electrical resistivity measurements [see Fig. 2 and Fig. 7(a)]. This finding implies that the observed superconductivity has a filamentary character and most probably spurious origin (see discussion in the next section).

D. Superconductivity

Figure 7(a) presents the low-temperature electrical resistivity of single-crystalline SrAgBi taken with electric current flowing in the ab plane and external magnetic fields applied along the c axis. Importantly, the experiment was carried out on the very same sample that was probed by heat capacity measurement (compare the data shown in Fig. 6). In the absence of magnetic field, a broad transition (width of ~ 0.8 K) to the zero-resistance state is observed with an on-

set at 2.9 K. In finite fields, this anomaly shifts to lower temperatures in a manner expected for superconductors. The critical temperature, defined by a drop in the magnitude of the resistivity by 10% in respect to its normal state value at 3 K, amounts to $T_c = 2.7$ K. Figure 7(b) displays the evolution of T_c with increasing field strength, in the form of $\mu_0 H_{c2}$ versus $t = T/T_c$, where $\mu_0 H_{c2}$ represents the upper critical field. As can be inferred from this figure, the experimental data can be approximated by the Ginzburg-Landau (GL) empirical formula, $\mu_0 H_{c2}(T) = \mu_0 H_{c2}(0) \frac{(1-t^2)}{1+t^2}$, with rather large $\mu_0 H_{c2}(0) \approx 2.4$ T. The latter value implies the superconducting coherence length $\xi(0) = [\Phi_0/2\pi H_{c2}(0)]^{1/2} \approx 117$ Å (Φ_0 is the flux quantum). These values are similar, e.g., to those reported recently for LuPdBi [$\mu_0 H_{c2}(0) \approx 2.2$ T and $\xi(0) \approx 120$ Å [48]].

Figure 7(c) shows the magnetic susceptibility (χ) measured for the same SrAgBi crystal in a small field of 2 mT in zero-field-cooled (ZFC) and field-cooled (FC) regimes. The emergence of a diamagnetic signal below 2.9 K is fully consistent with the $\rho(T)$ data and supports the superconductivity scenario. However, it should be noted that the maximum superconducting volume fraction is only $\sim 1.3\%$, which excludes the bulk character of the Meissner state, in concert with

the absence of any superconductivity-related anomaly on the $C_p(T)$ curve. There is a clear FC-ZFC bifurcation below T_c , and the increase in $\chi(T)$ occurring in the FC mode is likely due to the paramagnetic Meissner effect, usually observed for type-II superconductors with strong pinning [49]. In the magnetic field dependence of the magnetization (M) measured at 2 K [see the inset to Fig. 7(c)] one can recognize three distinct regions, outlined by the critical fields, $\mu_0 H_{c1} \approx 2$ mT, $\mu_0 H_{c2} \approx 20$ mT, and $\mu_0 H_{c3} \approx 140$ mT, which represent the Meissner state, mixed state, and normal state, respectively. The value of $\mu_0 H_{c2}$ is much smaller than that derived from the $\rho(T)$ data, and this inconsistency points to a filamentary character of the Cooper pairs formation in the single crystal measured.

The absence of superconducting transition in the specific heat of SrAgBi and the very small volume fraction of the superconducting signal estimated from the magnetic susceptibility data suggest that the superconductivity found in the single crystals examined has an extrinsic nature and probably originates from some unidentified impurity. The extrinsic nature of superconductivity is further confirmed from the sample dependence of T_c and variation in the superconducting volume fraction. Figure 7(d) represents the low-temperature ρ and χ measurements in the superconducting region for the several different crystals marked as C2, C4, C5, and C6 respectively. The results of the measurements show different T_c values and almost three times smaller superconducting volume fraction than the crystal C1. Yet the nature of the impurity phase responsible for superconductivity remains unknown within the experimental limits of our XRD and EDX data. The possibility of superconductivity from any of Sr, Ag, and Bi can be easily ruled out as none of these superconducts down to 2 K at ambient pressure. In the literature, superconductivity is reported in SrBi₃ at 5.6 K [50]. Although our powder XRD data do not show any SrBi₃ impurity phase, its T_c is also higher compared to the T_c values observed in SrAgBi. However, it is difficult to completely rule out the possibility of contamination by SrBi₃ phase because powder XRD has the limitation of detecting phase less than 1%.

IV. CONCLUSIONS

We have investigated the magnetotransport properties of single crystals of the putative topological semimetal SrAgBi in the temperature range 2–300 K with electric current flowing within the crystallographic ab plane and magnetic fields up to 9 T applied along the c axis. The electrical resistivity exhibits metallic behavior with a broad transition to the superconducting state occurring near 2.9 K. The onset of superconductivity has also been observed in the magnetic susceptibility study; however the superconducting volume fraction has been estimated as very small. Furthermore, no superconducting transition has been detected in the heat capacity measurement, and these findings suggest a filamentary nature of the Cooper pairing that can be attributed to a small amount of some unknown superconducting impurity present in the single crystals studied.

We have found that single-crystalline SrAgBi exhibits a very small transverse magnetoresistance of few percent at 5 K in 9 T, which reflects its semimetallic character with extreme charge imbalance. The Hall data have shown strong dominance of holes with carrier density of $\sim 10^{20}$ cm⁻³ and mobility of $\sim 10^2$ cm²/(Vs), hardly changing over the entire temperature range covered. The magnetoresistance data taken in small magnetic fields reveal the WAL effect at low temperatures. The robustness of WAL effect can be considered as an indication of a Weyl state that has been predicted theoretically [6,21]. The topological surface states form in a hole-dominated semimetal, but survive because of the relatively low mobility of carriers associated with the bulk states.

ACKNOWLEDGMENTS

We thank D. Ram, K. Wochowski, and T. Romanova for their assistance in crystal growth. Z.H. acknowledges Polish National Agency for Academic Exchange (NAWA) for Ulam Fellowship and Science and Engineering Research Board, Government of India (Grant No. CRG/2018/000220) for research support.

-
- [1] S. Murakami, *New J. Phys.* **13**, 105007 (2011).
 - [2] Y. Xia, D. Qian, D. Hsieh, L. Wray, A. Pal, H. Lin, A. Bansil, D. Grauer, Y. S. Hor, R. J. Cava, and M. Z. Hasan, *Nat. Phys.* **5**, 398 (2009).
 - [3] M. Z. Hasan and C. L. Kane, *Rev. Mod. Phys.* **82**, 3045 (2010).
 - [4] M. Konig, H. Buhmann, L. W. Molenkamp, T. Hughes, C.-X. Liu, X.-L. Qi, and S.-C. Zhang, *J. Phys. Soc. Jpn.* **77**, 031007 (2008).
 - [5] M. K. Hooda and C. S. Yadav, *Phys. Rev. B* **98**, 165119 (2018).
 - [6] T.-C. Ma, J.-N. Hu, Y. Chen, L. Shao, X.-R. Hu, and J.-B. Deng, *Mod. Phys. Lett. B* **35**, 2150181 (2021).
 - [7] Z. K. Liu, B. Zhou, Y. Zhang, Z. J. Wang, H. M. Weng, D. Prabhakaran, S.-K. Mo, Z. X. Shen, Z. Fang, X. Dai *et al.*, *Science* **343**, 864 (2014).
 - [8] E. Emmanouilidou, B. Shen, X. Deng, T.-R. Chang, A. Shi, G. Kotliar, S.-Y. Xu, and N. Ni, *Phys. Rev. B* **95**, 245113 (2017).
 - [9] S. Sasmal, R. Mondal, R. Kulkarni, A. Thamizhavel, and B. Singh, *J. Phys.: Condens. Matter* **32**, 335701 (2020).
 - [10] X. Huang, L. Zhao, Y. Long, P. Wang, D. Chen, Z. Yang, H. Liang, M. Xue, H. Weng, Z. Fang, X. Dai, and G. Chen, *Phys. Rev. X* **5**, 031023 (2015).
 - [11] J. Xiong, S. K. Kushwaha, T. Liang, J. W. Krizan, M. Hirschberger, W. Wang, R. J. Cava, and N. P. Ong, *Science* **350**, 413 (2015).
 - [12] H.-Z. Lu and S.-Q. Shen, *Phys. Rev. B* **92**, 035203 (2015).
 - [13] M. N. Ali, L. Schoop, C. Garg, J. M. Lippmann, E. Lara, B. Lottsch, and S. Parkin, *Sci. Adv.* **2**, e1601742 (2016).
 - [14] H.-P. Sun and H.-Z. Lu, *Front. Phys.* **14**, 33405 (2019).
 - [15] H. Yao, M. Zhu, L. Jiang, and Y. Zheng, *J. Phys.: Condens. Matter* **30**, 285501 (2018).
 - [16] Y. W. Li, H. J. Zheng, Y. Q. Fang, D. Q. Zhang, Y. J. Chen, C. Chen, A. J. Liang, W. J. Shi, D. Pei, L. X. Xu *et al.*, *Nat. Commun.* **12**, 2874 (2021).

- [17] Y. Li, Q. Gu, C. Chen, J. Zhang, Q. Liu, X. Hu, J. Liu, Y. Liu, L. Ling, M. Tian *et al.*, *Proc. Natl. Acad. Sci. USA* **115**, 9503 (2018).
- [18] Y. Xing, Z. Shao, J. Ge, J. Luo, J. Wang, Z. Zhu, J. Liu, Y. Wang, Z. Zhao, J. Yan *et al.*, *Nat. Sci. Rev.* **7**, 579 (2020).
- [19] C. Chen, Z. Su, X. Zhang, Z. Chen, and X.-L. Sheng, *J. Phys. Chem. C* **121**, 28587 (2017).
- [20] K. Nakayama, Z. Wang, D. Takane, S. Souma, Y. Kubota, Y. Nakata, C. Cacho, T. Kim, S. A. Ekahana, M. Shi *et al.*, *Phys. Rev. B* **102**, 041104(R) (2020).
- [21] C. K. Barman, C. Mondal, B. Pathak, and A. Alam, *Phys. Rev. Materials* **4**, 084201 (2020).
- [22] B. Singh, S. Mardanya, C. Su, H. Lin, A. Agarwal, and A. Bansil, *Phys. Rev. B* **98**, 085122 (2018).
- [23] S. Mardanya, B. Singh, S.-M. Huang, T.-R. Chang, C. Su, H. Lin, A. Agarwal, and A. Bansil, *Phys. Rev. Materials* **3**, 071201(R) (2019).
- [24] C. Mondal, C. K. Barman, A. Alam, and B. Pathak, *Phys. Rev. B* **99**, 205112 (2019).
- [25] S. Xu, H. Wang, Y.-Y. Wang, Y. Su, X.-Y. Wang, and T.-L. Xia, *J. Cryst. Growth* **531**, 125304 (2020).
- [26] Q. Zhu, Q. Wang, L. Li, Z. Yang, J. Yang, B. Chen, C. Cao, H. Wang, and J. Du, *Phys. Rev. B* **104**, 144305 (2021).
- [27] R. Singha, A. Kumar Pariari, B. Satpatia, and P. Mandala, *Proc. Natl. Acad. Sci. USA* **114**, 2468 (2017).
- [28] I. A. Leahy, Yu-P. Lin, P. E. Siegfried, A. C. Treglia, J. C. W. Song, R. M. Nandkishore, and M. Lee, *Proc. Natl. Acad. Sci. USA* **115**, 10570 (2018).
- [29] T. Liang, Q. Gibson, M. N. Ali, M. Liu, R. J. Cava, and N. P. Ong, *Nat. Mater.* **14**, 280 (2015).
- [30] O. Pavlosiuk, P. Swatek, D. Kaczorowski, and P. Wiśniewski, *Phys. Rev. B* **97**, 235132 (2018).
- [31] H.-Y. Yang, T. Nummy, H. Li, S. Jaszewski, M. Abramchuk, D. S. Dessau, and F. Tafti, *Phys. Rev. B* **96**, 235128 (2017).
- [32] J. He, C. Zhang, N. J. Ghimire, T. Liang, C. Jia, J. Jiang, S. Tang, S. Chen, Y. He, S.-K. Mo *et al.*, *Phys. Rev. Lett.* **117**, 267201 (2016).
- [33] S. Singh, V. Süß, M. Schmidt, C. Felser, and C. Shekhar, *J. Phys. Materials* **3**, 024003 (2020).
- [34] A. Laha, P. Rambabu, V. Kanchana, L. Petit, Z. Szotek, and Z. Hossain, *Phys. Rev. B* **102**, 235135 (2020).
- [35] L.-M. Wang, S.-En Lin, D. Shen, and I.-N. Chen, *New J. Phys.* **23**, 093030 (2021).
- [36] H. Nakamura, D. Huang, J. Merz, E. Khalaf, P. Ostrovsky, A. Yaresko, D. Samal, and H. Takagi, *Nat. Commun.* **11**, 1161 (2020).
- [37] X. Zhang, J. M. Woods, J. J. Cha, and X. Shi, *Phys. Rev. B* **102**, 115161 (2020).
- [38] J. Chen, H. Li, B. Ding, Z. Hou, E. Liu, X. Xi, G. Wu, and W. Wang, *Appl. Phys. Lett.* **116**, 101902 (2020).
- [39] D. Neumaier, K. Wagner, S. Geißler, U. Wurstbauer, J. Sadowski, W. Wegscheider, and D. Weiss, *Phys. Rev. Lett.* **99**, 116803 (2007).
- [40] M. Liu, J. Zhang, C.-Z. Chang, Z. Zhang, X. Feng, K. Li, K. He, L.-L. Wang, X. Chen, X. Dai *et al.*, *Phys. Rev. Lett.* **108**, 036805 (2012).
- [41] H. Afzal, S. Bera, A. K. Mishra, M. Krishnan, M. Mishra, R. Venkatesh Patidar, and V. Ganesan, *J. Supercond. Nov. Magn.* **33**, 1659 (2020).
- [42] S. Hikami, A. I. Larkin, and Y. Nagaoka, *Prog. Theor. Phys.* **63**, 707 (1980).
- [43] O. Pavlosiuk, D. Kaczorowski, and P. Wiśniewski, *Sci. Rep.* **5**, 9158 (2015).
- [44] A. Laha, S. Malick, R. Singha, P. Mandal, P. Rambabu, V. Kanchana, and Z. Hossain, *Phys. Rev. B* **99**, 241102(R) (2019).
- [45] O. Pavlosiuk, D. Kaczorowski, and P. Wiśniewski, *Phys. Rev. B* **94**, 035130 (2016).
- [46] C. M. Hurd, *The Hall Effect in Metals and Alloys* (Plenum, New York, 1972).
- [47] Y. Okamoto, T. Inohara, A. Yamakage, Y. Yamakawa, and K. Takenaka, *J. Phys. Soc. Jpn.* **85**, 123701 (2016).
- [48] G. Xu, W. Wang, X. Zhang, Y. Du, E. Liu, S. Wang, G. Wu, Z. Liu, and X. X. Zhang, *Sci. Rep.* **4**, 5709 (2014).
- [49] W. Braunisch, N. Knauf, V. Kataev, S. Neuhausen, A. Grütz, A. Kock, B. Roden, D. Khomskii, and D. Wohlleben, *Phys. Rev. Lett.* **68**, 1908 (1992).
- [50] A. Iyo, Y. Yanagi, T. Kinjo, T. Nishio, I. Hase, T. Yanagisawa, S. Ishida, H. Kito, N. Takeshita, K. Oka, Y. Yoshida, and H. Eisaki, *Sci. Rep.* **5**, 10089 (2015).